


Vector coding and place coding in hippocampus share a common directional signal

Received: 22 August 2023

Accepted: 25 November 2024

Published online: 05 December 2024

Yue-Qing Zhou^{1,7} , Vyash Puliyadi^{1,2,7}, Xiaojing Chen^{1,6}, Joonhee Leo Lee¹, Lan-Yuan Zhang³ & James J. Knierim^{1,2,4,5} 

Vector coding is a major mechanism by which neural systems represent an animal's location in both global and local, item-based reference frames. Landmark vector cells (LVCs) in the hippocampus complement classic place cells by encoding vector relationships between the organism and specific landmarks. How these place- and vector-coding properties interact is not known. We recorded place cells and LVCs using calcium imaging of the CA1 region of freely moving rats during cue-card rotation studies. Place fields rotated around the center of the platform to follow the cue rotation, whereas the fields of simultaneously recorded LVCs rotated by the same amount around the nearby landmarks. Some neurons demonstrated conjunctive coding of both classic place field properties and LVC properties. These results demonstrate that CA1 neurons employ a common directional input, presumably provided by the head direction cell system, to encode animals' locations in both world-centered and landmark-centered reference frames.

Place cells in the CA1 region of the hippocampus are spatially tuned to represent an animal's location in an environment. This tuning is achieved both by triangulating the animal's location relative to allothetic landmarks and by integrating the animal's speed and direction of travel to continuously update an internal representation of the animal's location; the latter is known as path integration^{1,2}. Place cells³, grid cells⁴, and head direction cells^{5,6}, among other functional cell types^{7–11} are postulated to contribute to the formation of this internal, cognitive map, which not only supports flexible navigation but also serves as a spatiotemporal framework that binds together various components of an experience and allows the experience to be stored and retrieved as an episodic memory^{3,12,13}.

Objects have been used to study both the mechanisms that form the spatial framework as well as the binding of nonspatial information onto the map. Regarding the former, objects can be used as directional

landmarks to set the orientation of the internally coherent map when the objects are placed at the periphery of an environment¹⁴. Centrally located objects are less effective in this role¹⁴. Regarding the latter, flexible spatial navigation and adaptive behavior require animals to embed the landmarks and other features of the environment into the world-centered cognitive map, in order to populate the map with information about what the animal experiences in the environment. In support of this binding role, objects modulate the firing pattern of place cells within their firing fields^{15,16}. For example, “misplace cells”³ fire in a specific location only when an unexpected object or reward appears in that place, or when an expected object or reward is missing.

Animals can use individual landmarks to navigate to a specific location^{17,18}. Exploration of landmarks modulates the firing rates of CA1 pyramidal cells^{19–21} and lateral entorhinal cortex (LEC) cells^{22,23}. However, those studies do not provide strong evidence that rats generate

¹Zanvyl Krieger Mind/Brain Institute, Johns Hopkins University, Baltimore, MD, USA. ²Department of Psychological and Brain Sciences, Johns Hopkins University, Baltimore, MD, USA. ³Department of Anatomy and Neurobiology, University of Maryland School of Medicine, Baltimore, MD, USA. ⁴Kavli Neuroscience Discovery Institute, Johns Hopkins University, Baltimore, MD, USA. ⁵The Solomon H. Snyder Department of Neuroscience, Johns Hopkins University School of Medicine, Baltimore, MD, USA. ⁶Present address: Brain Research Centre and Department of Biology, Southern University of Science and Technology, Shenzhen, Guangdong Province, China. ⁷These authors contributed equally: Yue-Qing Zhou, Vyash Puliyadi. ✉ e-mail: zhouyq@jhu.edu; jkknierim@jhu.edu

spatial representations bound to these local landmarks. The discovery in the hippocampus of landmark vector cells (LVCs), a specific type of object representation that encodes the animal's location as a vector specifying the animal's distance and angle to discrete landmarks²¹, first confirmed the hypothesis of McNaughton et al.²⁴ that some place cells could exhibit such properties^{21,25}. Other spatially selective cell types that integrate landmark information into vector representations have subsequently been reported, such as object vector cells in the medial entorhinal cortex (MEC)²⁶, vector trace cells in the subiculum²⁷, and goal-vector cells in the hippocampus^{28,29}.

Although various types of information influence the firing patterns of place cells, the orientation of the cognitive map in the hippocampus is thought to be controlled largely by the head direction cell system^{30–32}. It is unknown whether LVCs derive the direction component of their vectors from the same source as the place cell system. To address this question, we trained rats to forage on an open platform with varying numbers of landmarks and utilized the miniscope calcium imaging technology in freely behaving rats. We analyzed the responses of simultaneously recorded place cells and LVCs in the hippocampus when a salient cue card was rotated around the open field. The results showed that the firing fields of place cells and LVCs rotated by similar degrees relative to the center of the environment and relative to the nearby landmark, respectively, suggesting that place cells and LVCs share a common directional input to anchor their world-centered and landmark-centered firing fields.

Results

The characterization of place cells in freely moving rats with calcium imaging

We performed in vivo, single photon (1P) calcium imaging in rats with head-mounted miniscopes³³ as they foraged for irregularly scattered

food rewards on a square platform surrounded by a circular, black curtain (Fig. 1a). A large cue card was placed on the curtain to serve as the only salient, directional cue in the environment. Most studies using in vivo calcium imaging have been conducted in mice, with only a limited number being carried out on rats using head-mounted miniscopes^{34–38}. Therefore, we optimized surgery procedures to successfully apply in vivo calcium imaging to rats (Fig. 1c; see Methods for details). To validate our miniscope recordings against published electrophysiological studies of place cells³⁹, we characterized the proportions of active CA1 cells that had place fields in our experiment. To avoid counting the same cells multiple times over days, we analyzed the recordings only from the first session of recordings for each rat for this analysis. In these sessions, we recorded the calcium activity from 1547 CA1 neurons from 8 rats, of which 770 were defined as active cells (~50%), and 517 (~33%) were defined as place cells (see Methods for definitions of active cells and place cells). Although the total number of cells recorded decreased across sessions, the percentage of the place cells was relatively stable across sessions^{40,41}. These results are consistent with previous electrophysiological and IEG studies in rats that estimate that the percentage of CA1 cells that have place fields in a given environment ranges from ~33% to 50%, depending on the experimental task and environment^{39,42–45}.

Landmark-vector fields in CA1 hippocampus with calcium imaging recordings

In addition to place cells, we identified LVCs in the calcium imaging recordings (Fig. 2). It can be challenging to determine whether a firing field is a place field or an LV field in a single session, particularly when there is only one landmark on the platform or if the cell has a single firing field. Therefore, we often visually identified LVCs based on their

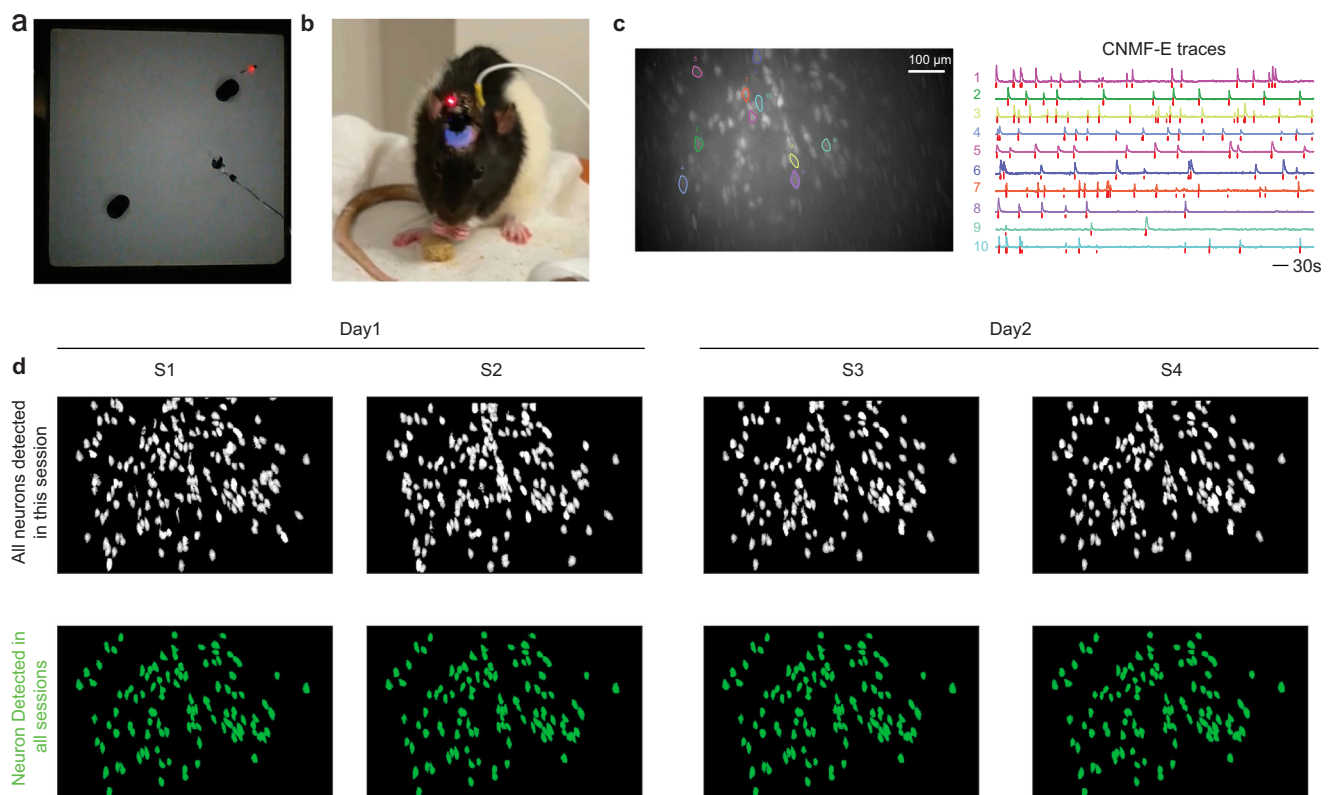


Fig. 1 | Experimental setup. **a** Recording square platform (107 × 107 cm) with 2 objects (large black items). The recording cable and head stage are also visible. **b** Rat with a head-mounted miniscope obtained from the UCLA open-source miniscope consortium (http://miniscope.org/index.php/Main_Page). **c** Z projection stacking of a raw calcium imaging video (left) and extracted fluorescence

traces (right, colors correspond to colored outlines of cells at left, red ticks below the fluorescence traces represent the deconvolved calcium events corresponding to putative spiking events). **d** Longitudinal registration across multiple days. Neurons colored in white represent those detected in each individual session (top), while those in green denote neurons detected across all sessions (bottom).

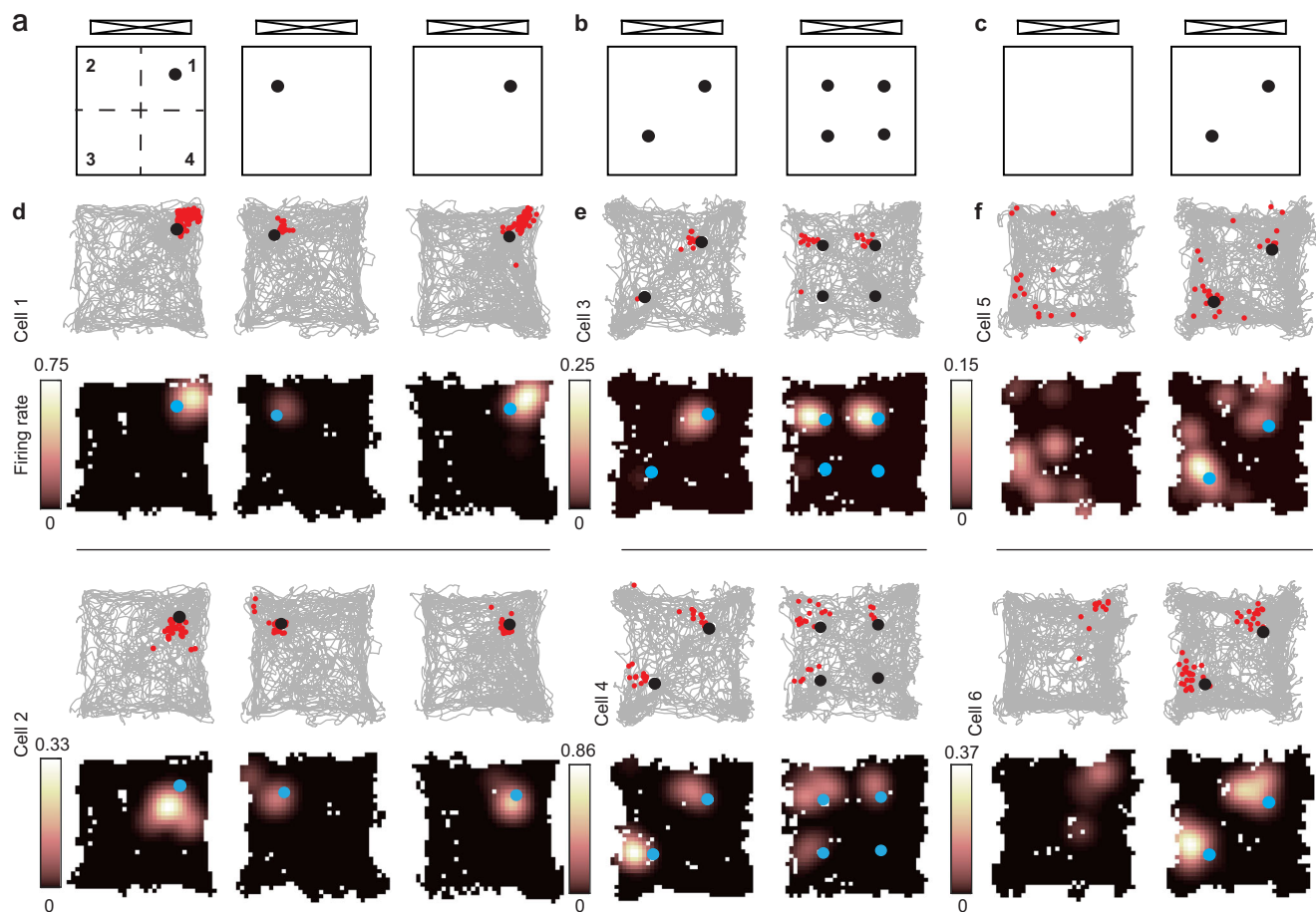


Fig. 2 | Identification of LVCs with calcium imaging recording in freely moving rats. **a–c** Schematic of three experimental configurations. **d** Two examples of LV fields that follow the movement of the landmark. (Top) Gray: rats' trajectory; red: locations of the rat when calcium events were detected. Black dots indicate the locations of objects. (Bottom) Occupancy-normalized calcium firing rate maps; blue dots show the locations of objects. **e** Two example cells showing that additional new objects cause the addition of a corresponding LV field with the same direction and distance relative to their anchoring landmarks. In the first session, Cell 3 had a strong LV field near the landmark in quadrant 1 and a single calcium transient near the landmark in quadrant 3; the single transient occurred at the same orientation relative to the quadrant 3 landmark as the place field relative to the quadrant 1 landmark. In the second session, in which 2 new landmarks were introduced, strong LV fields formed near both landmarks in quadrants 1 and 2, and another transient near the landmark in quadrant 3; the cell did not show any

detectable calcium activity near the landmark in quadrant 4. Cell 4 formed strong LV fields in the first session near both landmarks and added a new LV field near the landmark in quadrant 2 in the second session. **f** Two examples of adding two landmarks to an open field causing the appearance of two LV fields. Cell 5 displayed weak, diffuse activity primarily in quadrant 3. In the second session, two landmarks were introduced, and the cell was active at the same orientation and distance for both landmarks, along with diffuse firing at other locations in the environment. Cell 6, from the same recording session, formed a firing field near the corner of quadrant 1 in the first session; in the second session, the firing field was captured by the landmark (i.e., it moved toward the landmark) in quadrant 1 and formed another LV field near the landmark in quadrant 3. The second session was the rat's first experience with objects on the platform. For each panel, **d–f**, the example cells were recorded simultaneously.

firing properties across sessions⁴⁶. For example, in one experiment, a landmark vector field was identified because it maintained the same direction and distance relative to a landmark when the landmark's location was changed (Fig. 2a, d). In another experiment, additional landmarks were placed in an environment (Fig. 2b), and new firing fields formed that had the same bearing and distance to a subset of the new landmarks as the fields had to the original landmarks in the first session (Fig. 2e).

The third experiment started with an open platform for the first session, and novel objects were introduced to the platform in the second session (Fig. 2c). Landmark-vector fields were evident in the rats' first trajectories through the field near the landmarks (Fig. 2f; Supplementary Movie 1). These results demonstrate that in vivo calcium imaging techniques can be reliably applied to identify LVCs in rats' hippocampus, similar to our previous extracellular electrophysiological study²¹, and that LVCs do not necessarily require experience to develop their vector fields.

Control of place cell and LVC firing fields by rotation of a salient cue card

To investigate how the distal cues affect the landmark vector representations, the location of the cue card relative to the center of the square platform was rotated between sessions (Fig. 3a), using a classic test of cue control over place cells⁴⁷. In the first (standard) session, the cue was positioned north of the platform, at the same location as during prior training sessions. In the second (rotation) session, the cue was shifted toward the west of the platform in between sessions. Two local landmarks were located in the centers of quadrants 1 and 3 of the platform. As expected, the spatially tuned firing fields of place cells tended to rotate $\sim 90^\circ$ relative to the center of the platform when the cue card was rotated (Fig. 3b, Supplementary Fig. 4b). Importantly, LVCs also rotated their firing fields $\sim 90^\circ$, but the rotation was anchored to the nearby local landmark instead of the center of the platform (Fig. 3c; Supplementary Fig. 4c). We conducted cue card rotations back to the original position as a control for two rats, and

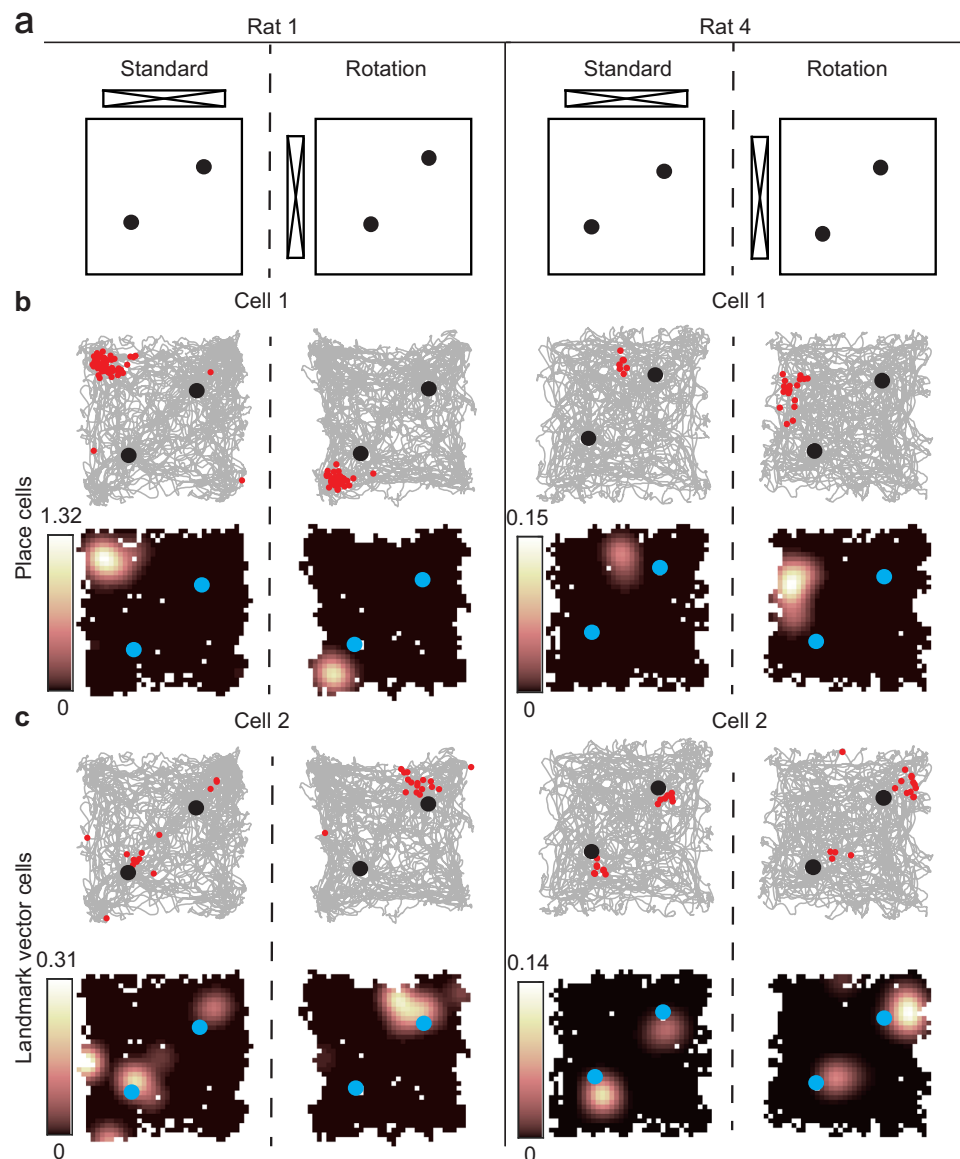


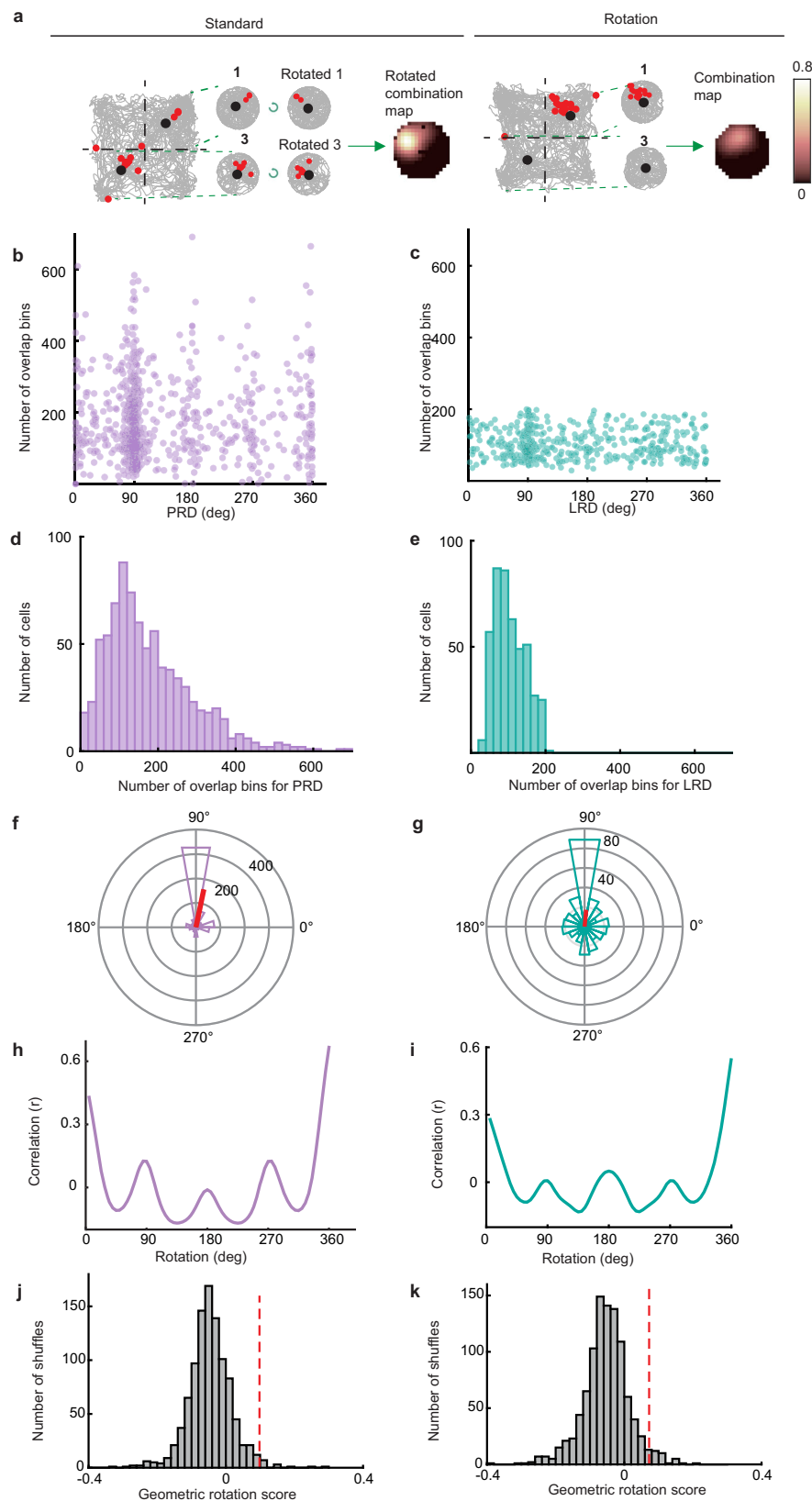
Fig. 3 | Examples of place cell and LVC responses when a salient cue card was rotated. **a** Experimental configurations. **b** Examples of place cells from two rats. The place fields rotated -90° relative to the center of the platform when the salient cue was rotated 90° . **c** Examples of LVCs from two rats, recorded simultaneously with the place cells of (b). Cell 2 from rat 1 showed LV responses to both landmarks

in the first session, with its firing field to the northeast of each landmark. In the rotation session, the cell now fired to the northwest of the landmark in quadrant 1 and it lost its firing field in quadrant 3. In contrast, cell 2 from rat 4 showed firing fields to the southeast of both landmarks in the standard session. The firing fields rotated to the northeast of both landmarks in the rotation session.

both LV fields and place fields typically rotated back to their original locations (Supplementary Fig. 2). However, due to the photobleaching-induced reduction in neuronal number in the third session, we typically limited our recordings to two sessions per day.

We performed modified versions of the standard rotation correlation analysis^{47–49} to quantify the degree of rotation of place fields and LV fields relative to the platform center and relative to the landmark locations. It was not always straightforward to define algorithmically a field as a place field vs. an LV field in these experiments, as the firing patterns were often complex and variable, especially when there were multiple landmarks in the environment and complex responses to cue rotations (e.g., some LV fields turning on or off, or jumping from one landmark to another). We thus chose to measure the degree of rotation of all firing fields (both putative place fields and putative landmark vector fields) around the center of the platform and around the centers of the landmarks and analyzed the population statistics of these measures to look for statistical effects from the entire cell population

(see Supplementary Fig. 7 for secondary analyses of putative individual LVCs identified by subjective, visual inspection). To calculate rotations relative to the center of the platform, we rotated the rate map of the standard session in 1° increments and, for each increment, calculated the number of overlapping spatial bins with non-zero firing rate in both the rotated standard session and the cue manipulation session. The platform-centered rotation degree (PRD) was defined as the rotation angle that had the maximum number of overlapping spatial bins (Supplementary Fig. 3, middle column). For rotations relative to the landmarks, we extracted a circular rate map (radius = 24 cm) centered on each landmark, to minimize the contribution of calcium events unrelated to that landmark (e.g., firing at the corners of the platform; Fig. 4a). Because LV fields could be anchored to different landmarks in different sessions (e.g., Supplementary Fig. 3c, left column, Supplementary Fig. 4c, d; also ref. 21), we first averaged the firing rate maps of the two landmark-centered circular rate maps (creating combination maps; Fig. 4a and Supplementary Fig. 3). We performed the same



rotation analysis on these circular rate maps as for the PRD and calculated the landmark-centered rotation degree (LRD) as the rotation angle that maximized the overlap of non-zero firing rate bins between the standard and rotation session combination maps (Supplementary Fig. 3, right column). Because some putative LV fields produced as few

as 1 transient near the landmark (e.g., Fig. 2b), we analyzed all cells that had at least one calcium event in both sessions.

On average, the degree of rotation of firing fields relative to the center of the platform equaled the degree of rotation of the landmark-centered firing fields relative to the landmarks. The angle of the mean

Fig. 4 | Landmark-vector cell firing fields are controlled by the cue card but anchored to the nearby landmarks. **a** Circular rate maps (24 cm radius) cut out from quadrants that contain landmarks (1 and 3) are incrementally rotated relative to the landmarks and merged at each increment to generate the rotated combination maps (90° rotation illustrated here). Each rotated combination map (left, Standard) was then compared to the combination map of the rotation session (right, Rotation). **b** Scatter plot shows the PRD and corresponding maximum numbers of overlap bins for all cells. **c** Scatter plot shows the LRD and corresponding maximum overlap bins for cells that had activity in either circular rate maps 1 or 3 in both sessions. **d** The distribution of maximum overlap bins from **(b)**. **e** The distribution of maximum numbers of overlap bins from **(c)**. **f** Polar plot of the distribution of PRD (red line denotes the direction and magnitude of the mean resultant vector: mean angle = 78.2°). **g** Polar plot of the distribution of LRD (red

line denotes the direction and magnitude of the mean resultant vector: mean angle = 84.2°). **h** Autocorrelation plot of PRD. We rotated the polar plot of **f** in steps of 5° and computed the correlation between each rotated vector and the original vector. **i** Autocorrelation plot of LRD, similar to that of PRD. **j** The significance of the geometric rotation score was determined by creating a null distribution by randomly assigning a value varying from 1° to 360° to each cell and calculating the geometric rotation score for those permutations. The red dashed line indicates the actual geometric rotation score, which is greater than the 95th percentile of the null distribution (one-sided test, $P < 0.05$). **k** The significance of the geometric rotation score for LRD, performed similarly to that for PRD. The red dashed line indicates the actual geometric rotation score, which is greater than the 95th percentile of the null distribution (one-sided test, $P < 0.05$). Source data are provided as a Source Data file.

vector of PRD from the 821 neurons that had at least one calcium event in both sessions was $78.2^\circ \pm 5.4^\circ$ (Fig. 4f, $r = 0.48$; Rayleigh's test, $P < 0.001$). Of these 821 neurons, 452 had activity in the circular rate maps of quadrants 1 or 3 in both sessions; the mean vector angle of LRD from these 452 neurons was $84.2^\circ \pm 19.7^\circ$ (Fig. 4g, $r = 0.19$; Rayleigh's test, $P < 0.001$). There was no significant difference between the PRD and LRD medians (circular analog of Kruskal–Wallis test, $\chi^2 = 0.14$, $P = 0.70$). These findings suggest that place field representations and LV representations share the same directional information, each one undershooting the rotation of the cue card by $\sim 10^\circ$ (in agreement with prior studies of head direction cells and place cells under cue-conflict situations^{50–52}). Although both LRD and PRD showed mean rotation angles controlled by the cue card, both distributions showed a large number of points away from the 90° value corresponding to cue rotation; this result is expected, as we did not separate the cells into putative place cells and LVCs, as described above, and thus each cell type contaminated the results of the other while still allowing the overall population trends to be identified. The distribution of LRD values (Fig. 4g) was more dispersed than that of PRD values (Fig. 4f). Part of this dispersal may be due to the smaller size of the LV firing fields compared to standard place fields and also due to encroachment of place fields from the circular rate maps of quadrants 2 and 4 into the circular rate maps of quadrants 1 and 3 (Supplementary Fig. 3). The distributions of Fig. 4f, g demonstrate a 4-fold radial symmetry in PRD and LRD, respectively, suggesting that the square geometry of the environment influenced the rotation angles of the firing fields relative to the landmarks. To quantify this effect, we measured the periodicity of the PRD and LRD polar plots of Fig. 4f, g by computing an autocorrelation of each of these plots. The distributions of PRD and LRD were rotated in steps of 5°, and the correlation between each rotated distribution and its original was computed and smoothed with a Gaussian-weighted moving average filter with a window of length 10. If the PRD or LRD was influenced by the geometry of the platform, the values of the correlations should be greater at 90°, 180°, and 270° rotations than for 45°, 135°, 225°, and 315°. As predicted, the correlations peaked at multiples of 90° (Fig. 4h, i). Analogous to the standard measure used to measure the sixfold rotational symmetry of grid cells⁵³, we defined the geometric rotation score as the minimum value of the hypothesized peak correlations (90°, 180°, 270°) minus the maximum value of the hypothesized trough correlations (45°, 135°, 225°, 315°). To simulate a null distribution, we randomly assigned an integer value from 1° to 360° to each cell and calculated the geometric rotation score. The geometric rotation score of the observed data was 0.10 for PRD and 0.072 for LRD, which exceeded the 95th percentile values of the simulated null distributions, respectively (Fig. 4j, k; $P < 0.05$ and $P < 0.05$, respectively).

Since the analyses of Fig. 4 statistically verified the existence of landmark-vector properties in a subset of neurons across the population, we further explored the properties of individual LVCs by subjectively identifying them via visual inspection of the firing rate maps in cue card rotation experiments and tracked them across multiple days

(Supplementary Fig. 7a). Typically, the firing fields of LVCs rotated approximately 90° in cue card rotation experiments, or they maintained the same vector relationship relative to nearby landmarks in landmark translation or addition paradigms (Supplementary Fig. 7a). Some animals underwent the same experimental protocols multiple times due to variations in data quality, while others participated in additional exploratory experiments not described here, as they are beyond the scope of the current study. The mean vector angle of LRD for visually identified LVCs (75/821, 9%) in the cue card rotation experiment was $87.1^\circ \pm 20.1^\circ$ (Supplementary Fig. 7c, $r = 0.44$; Rayleigh's test, $P < 0.001$). When the locations of the landmarks were altered, among the 60 identified LVCs, 32 maintained the same number of LV fields, 14 LVCs exhibited an increase in LV fields, 11 showed a decrease, and 3 experienced a change in the landmark to which their firing fields were anchored (Supplementary Fig. 7b, left). Furthermore, when the cue card was rotated, 30 LVCs maintained the same number of LV fields and remained anchored to the original landmark, 14 LVCs exhibited an increase in LV fields, 12 LVCs showed a decrease in LV fields, and 19 LVCs experienced a jump in the landmark to which their firing fields were anchored (Supplementary Fig. 7b, right).

Conjunctive representations of landmark vector fields and place fields

Since LVCs and place cells, both exist in CA1 of the hippocampus and respond similarly to cue card rotations, we next investigated whether individual CA1 cells could show both classic place cell properties and LVC properties. Our results revealed a form of conjunctive coding in a subset of hippocampal place cells, in which an animal's location is represented by the same cell in both the world-centered frame (a standard place field) and in a landmark-centered frame (an LV field) (Fig. 5; Supplementary Fig. 4d, e; see Methods). In some cases, the cell displayed distinct subfields, each of which demonstrated either place field or LV properties (Fig. 5a: Rat 1_Cell1; Fig. 5b: Rat 3_Cell1). Alternatively, cells with a single firing field observed in the standard session could be divided into two distinct firing fields when the cue card was rotated, with one field anchored to the center of the platform and the other field anchored to the landmark (Fig. 5a: Rat 1_Cell 2; Fig. 5b: Rat 3_Cell 2). The representations of conjunctive landmark vectors and place cells were dynamic. Some LVCs emerged during the rat's first encounter with the landmarks (Supplementary Fig. 6a, Supplementary Movie 1), whereas other conjunctive cells developed their LV fields (Supplementary Fig. 4e) or lost their LV fields (Supplementary Fig. 4d) in later recording sessions or days. Figure 5c shows a scatter plot of the distribution of PRD relative to LRD for each cell that had a valid LRD value. Collapsing the data across each axis demonstrates that the most common response was $\sim 90^\circ$ for both measures. To address whether individual cells were more likely than chance to share this rotation amount between LRD and PRD, the difference between PRD and LRD was calculated for each cell; the distribution of this difference peaked at 0° (Fig. 5d). Of the cells that were active in quadrants that contained objects, 16.6% (75/451) were defined as a conjunctive place x LV cell in

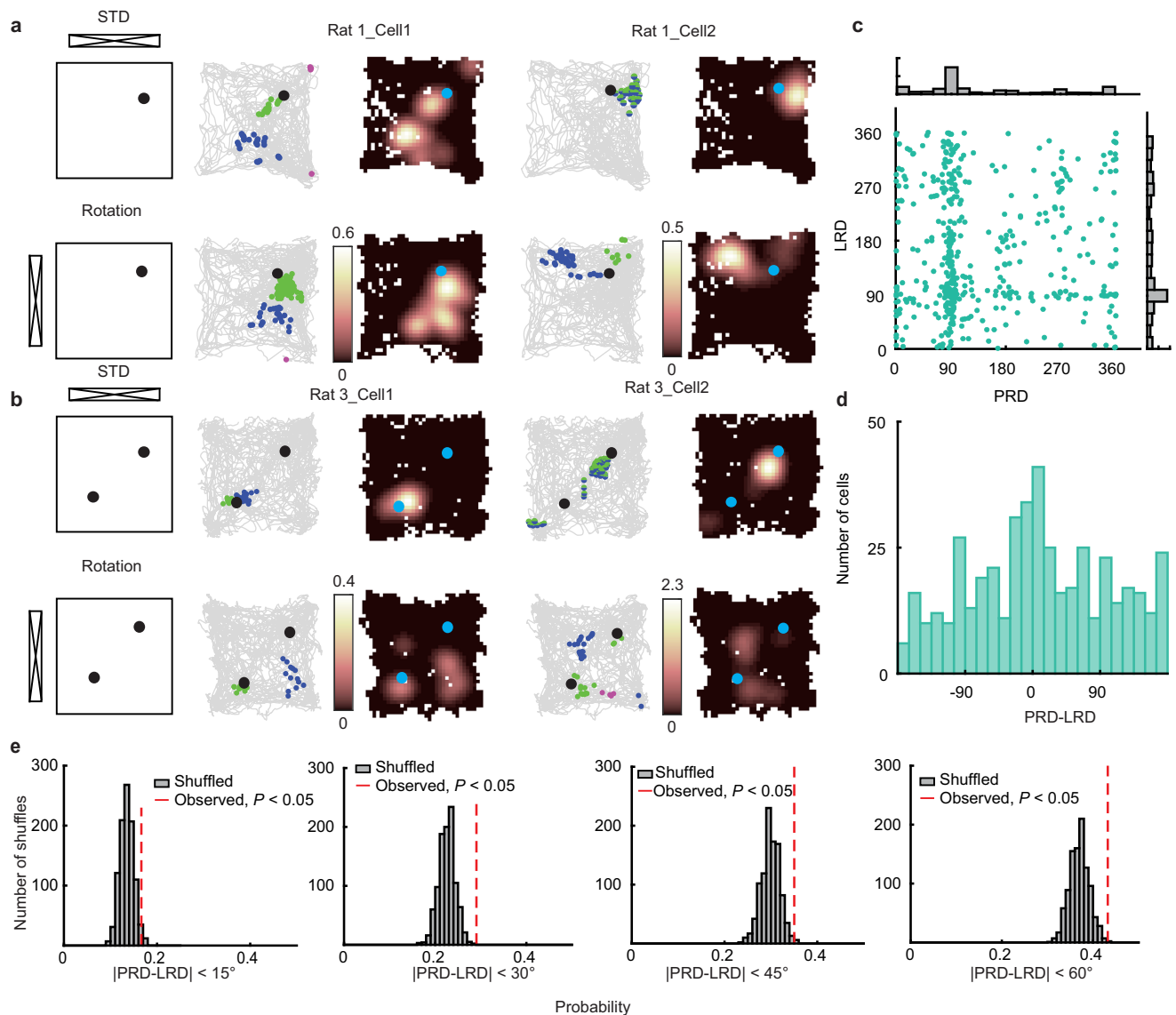


Fig. 5 | Conjunctive representations of LV fields and place fields. **a** Examples of two conjunctive place x LV cells with one landmark. In all panels, calcium events highlighted in blue denote place representations, in green denote LV representations, in purple mark other representations, and in half-green, half-blue indicate conjunctive firing fields that split into place and LV representations in the next session. Rat 1 Cell 1 had two firing fields in the standard session. In the rotation session, the green field rotated -90° around the landmark whereas the blue field rotated -90° relative to the platform center. Rat 1 Cell 2 had a single place field (blue-green dots) in the standard session, making it ambiguous as to whether it was a place field or an LV field. In the rotation session, the firing field split into two subfields, with one (green) rotating around the landmark and the other (blue) rotating around the platform center. **b** Example of two conjunctive place x LV cells with two landmarks. Rat 3 Cell 1 had an elongated field near the landmark in quadrant 3 in the standard session (denoted by green and blue dots). In the rotation

session, the field split in two, as a small subfield (green) rotated around the landmark and a larger subfield (blue) rotated around the center of the platform. Rat 3 Cell 2 had 2 fields in the standard session. The two subfields broke into 4 subfields in the cue-rotation session, rotating around the landmark (green) and the center of the platform (blue). **c** Scatter plot of PRD and LRD values for each cell. **d** Distribution of the difference between LRD and PRD for each cell. **e** A shuffled distribution of the difference between LRD and PRD for each cell was generated 1000 times by randomly assigning LRD values without replacement. The percentage of conjunctive representations, defined as those with $|PRD-LRD| < 15^\circ$ (left), 30° (left, middle), 45° (right, middle), or 60° (right), in each of those 1000 random distributions are plotted. The red dashed line indicates the observed data, which is outside the 95% confidence interval for each criterion (one-sided test, $P < 0.05$). Source data are provided as a Source Data file.

that the difference between the LRD and PRD for each cell was $<15^\circ$. Cells identified as conjunctive place x LV cells shared the same degree of rotation, which typically (but not necessarily) rotated $\sim 90^\circ$ in cue card rotation sessions (Supplementary Fig. 3p, t, x). To assess whether the population level conjunctive activity was random, we shuffled the LRD values of each cell by assigning randomly without replacement values from the distribution of LRDs to each cell. For each of the 1000 shuffles, the percentage of the cells showing conjunctive place x LV fields was computed using 4 criteria ($|PRD-LRD| < 15^\circ$, $|PRD-LRD| < 30^\circ$, $|PRD-LRD|$

$< 45^\circ$, and $|PRD-LRD| < 60^\circ$), to show that the significance was not due to choosing a specific criterion. The percentage of the conjunctive place x LV cells in the observed data was found to be above the 95th percentile of the null distribution for all criteria (Fig. 5e).

Landmarks enhance the stability of nearby firing fields across days

Place coding in hippocampal place cells can remain stable over long periods in rats^{46,54} (but see recent work showing representational drift,

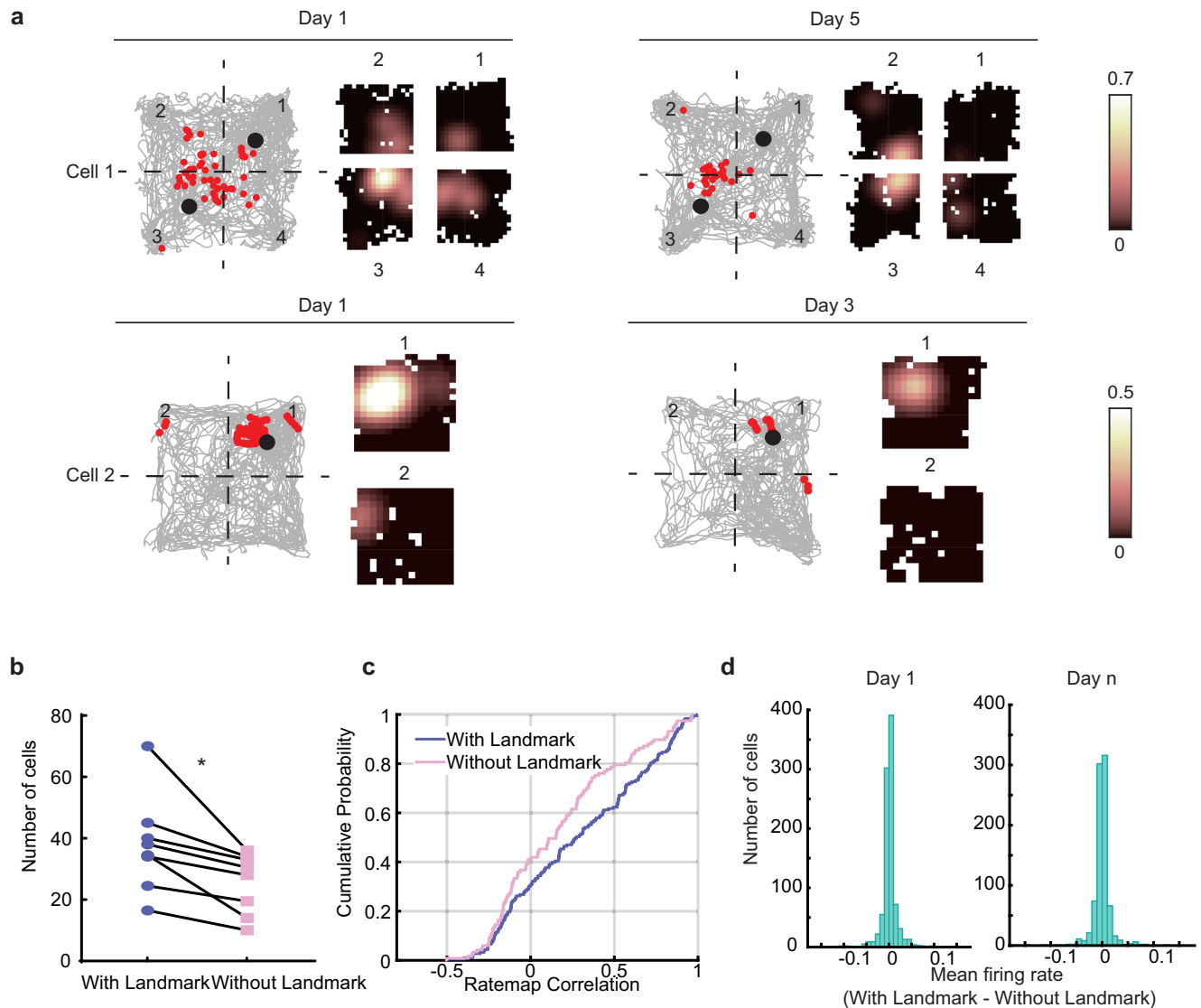


Fig. 6 | Landmarks enhance the stability of neuronal representation near the objects across days. **a** The number of consistently active cells and the correlation coefficients between each quadrant on day 1 and its corresponding quadrant on day n (where $n = 3, 5$, or 7 , depending on the rat) were computed for all the cells. For the experimental configuration with two landmarks (top), the number of cells with consistent activity across days was calculated as the average of these values for quadrants 1 and 3 and quadrants 2 and 4. Similarly, the correlation coefficients of the quadrant rate maps were calculated as the average of these values for quadrants 1 and 3 and quadrants 2 and 4. For the experimental configuration with only one landmark (bottom), we used only quadrants 1 and 2 to calculate the numbers of

consistently active cells across days and the rate map correlations across days.

b The number of cells from 8 rats exhibiting consistent responses near landmarks across multiple days is significantly greater than the number of cells showing consistent responses distant from landmarks ($t_7 = 3.4$, $P = 0.011$; two-sided paired t test). **c** Correlations between the quadrant rate map that contains landmarks are higher than the quadrant rate map without landmarks ($D = 0.184$, $P = 0.014$, two-sided two-sample Kolmogorov–Smirnov test). **d** There was a weak increase in the mean firing rates of neurons in quadrants with landmarks compared to quadrants without landmarks on day 1 but not on a later recording day. Source data are provided as a Source Data file.

e.g.,^{46,55}). Additionally, virtual objects enhance the stability of place cells near these objects in mice⁵⁶. Given that nearby landmarks offer an extra coordinate frame for animals to estimate their location, we hypothesized that nearby landmarks might increase the stability of spatial representations across days. We found that cells with signals in quadrants containing landmarks were more likely to maintain consistent activity in those quadrants across days compared to cells with signals in quadrants without landmarks. The number of neurons with at least one calcium transient in quadrant 1 or 3 on both day 1 and day n ($n = 3, 5$, or 7 , depending on the individual animal) was significantly higher than the number of neurons with at least one calcium transient on both days in quadrants without landmarks (2 and 4) on day 1 and day n (Fig. 6b; paired t test, $t_7 = 3.405$, $P = 0.011$). Moreover, the spatial correlations of the quadrant rate maps with landmarks

were higher than those without landmarks (Fig. 6c, two-sample Kolmogorov–Smirnov test, $D = 0.184$, $P = 0.014$). Therefore, local landmarks enhance the stability of the nearby neural representations across days. To compare the influence of the landmark on the mean firing rate in quadrants with and without landmarks, for each cell, its mean firing rate in the quadrants without landmarks was subtracted from the mean firing rate in the quadrants that contained landmarks. On day 1, the firing rates in quadrants with landmarks were slightly larger than the firing rates in quadrants without landmarks (Fig. 6d, left; Day 1: $t_{939} = 2.0$, $P = 0.048$; two-sided paired t test). However, no significant difference was observed on a later recording day (Fig. 6d, right; Day n : $t_{846} = 0.48$, $P = 0.63$, two-sided paired t test). Additionally, there was no significant difference in the subtraction between Day 1 and Day n ($t_{1786} = 1.78$, $P = 0.076$, two-sided t test), suggesting the

proximity of landmarks does not strongly change the firing rates of neurons at the population level.

Discussion

We recorded cells from CA1 in freely moving rats with varying numbers of landmarks in the environment to investigate whether the orientation of the place cell map and the directional component of LVCs share a common directional input. In agreement with previous studies in the hippocampus²¹, entorhinal cortex²⁶, and dentate gyrus⁵⁷, the fields of LVCs have the same vector relationship with multiple landmarks or maintain the same vector relationship relative to a landmark when the location of the landmark was changed. As expected, the orientation of the place field map was anchored to a global reference frame, as the rotation of a salient cue card in the periphery caused equivalent rotations of place fields around the center of the environment^{5,32}. In contrast, the LV fields were also controlled by the cue card but were anchored to the reference frame of the individual landmarks to which they were bound. This result was not obvious a priori, as there were a number of alternative hypotheses about how the directional components of place fields and LV fields might have reacted to the cue card (Supplementary Fig. 8). The identification of conjunctive place x LV cells suggests that individual neurons in CA1 have the capacity to encode both place fields and LV fields despite those two representations being anchored to two different coordinate frameworks. Finally, our results showed that the presence of landmarks enhanced the stability of nearby place fields across days.

LVCs encode animals' location in a landmark-centered frame

Place cells are thought to primarily encode space in an allocentric (i.e., world-centered) frame of reference^{3,58}, independent of egocentric spatial information such as the orientation of animals' bodies or head⁵⁹ (but see ref. 60–62 for exceptions). The firing rates of place cells can change in the presence of landmarks¹⁵, implicitly suggesting that place cells integrate information about landmarks in an allocentric frame of reference. However, LVCs represent landmarks in a completely different frame of reference than place cells; that is, LVCs are anchored to individual landmarks rather than to a global, world-based reference frame. The combination of representations of location in different reference frames may help the rat to evaluate the current location precisely⁶³. Similar to previous proposals about the roles of boundaries in correcting path integration errors^{11,63–66}, landmarks may pin the internal cognitive map to a specific location in the world. LVCs may also convey to downstream cells information about the rat's location relative to the landmark in terms of direction and distance, while the hippocampal population activity may provide information about what and/or where the landmark is in allocentric space^{15,67}.

Although a single cell can encode both place and landmark vector representations (Supplementary Fig. 6b, c), it is essential to consider whether they constitute functionally separate classes of cells or are instead different types of response of the same class of cells. For example, distinct cell types of the MEC (e.g., grid cells and object vector cells) are considered as functionally dedicated populations of cells that are anatomically distinct from each other²⁶; that is, a grid cell appears to always be a grid cell in any environment under normal conditions^{4,68}, and it is unlikely, if ever, to be an object vector cell²⁶. In contrast, individual pyramidal cells of the hippocampus can act as place cells under certain circumstances and time cells under other circumstances⁶⁹. Similarly, the dynamic transition seen between place cells and conjunctive place x LV cells in the current study (Fig. 5; Supplementary Fig. 4) suggests that LV fields and place fields may derive from the same anatomical set of cells that sometimes act as place cells and other times as LVCs. Regardless of whether a cell acts as a place cell or an LVC in a given environment, it appears to be controlled by a common orientation signal⁸. Thus, as Deshmukh and Knierim²¹ have argued previously, LVCs are better taken as

descriptions of different types of functional responses of CA1 neurons instead of a new type of cell in any anatomical or morphological sense. In agreement with their hypothesized mnemonic roles of associating arbitrary stimuli (spatial and nonspatial) in the service of episodic memory, hippocampal cells appear to show greater flexibility in their coding properties than MEC cells, for example.

Head direction cells are likely to set the orientation of the place cell map and the directional component of LVC vectors

Head direction cells are a major input to the hippocampal system⁷⁰. These cells increase their firing when the rats' head is pointing in a specific, allocentric direction, regardless of the animal's location^{70,71}. Place cells and head direction cells of the anterior dorsal thalamus are tightly coupled, in that rotation of a salient, distal cue causes the corresponding rotation of place fields and head direction tuning curves relative to the center of the environment^{32,51}. More importantly, under conditions in which place cells and head direction cells become decoupled from any external reference frame, they remain coupled to each other^{6,51}. This result demonstrates an internal coupling between these two types of cells, rather than independent control of place cells and head direction cells by external landmarks⁶⁴. Similarly, in the present study, place fields and LV fields were both strongly controlled by the rotation of a salient cue, although they both tended to under-rotate their firing fields by a similar amount. Place fields and LV fields also showed similar fourfold rotational symmetry, presumably influenced by the fourfold symmetry of the square platform. Because head direction cells also show such influences of environmental geometry^{72–75}, we hypothesize that the place cells and LVCs share a common directional input, most likely mediated by the head direction cell system. It is worth noting that the landmarks in the present study were radially symmetric; it would be of interest to determine in the future whether the directional component of the LV fields could decouple from the place field map orientation if the landmarks were asymmetric (i.e., if the rat's view of the landmark was different from different viewing angles) (Supplementary Fig. 8b: condition 3).

Landmarks stabilize the spatial coding in CA1 neurons

By tracking the same cells in the same environment over multiple days, we found that spatial representations near objects are more stable than representations farther from objects (Fig. 6). These results complement a recent demonstration that population firing rates can decode the presence or absence of objects with decoding accuracy dependent on distance to the object location⁶⁷. The firing fields of hippocampal neurons can be stable over days in a nonchanging environment^{54,76}, but recent work has unveiled a much larger degree of representational drift in place cells than was previously appreciated^{146,55}. Despite this representational drift, the hippocampal population still maintains the ability to represent different contexts in a sustained manner, as the parts of state space within which the representation drifts for one context appear to remain segregated from that part of state space within which the representation of the other context resides⁷⁷. Landmarks may serve as one of the contextual cues that limit the representational drift and keep the representation confined to a specific neighborhood of neural activity state space, preventing it from impinging on the neural neighborhood of another context. Therefore, landmarks may not only be represented in the hippocampus as individual items that occupy specific locations on the cognitive map, but the relative stability of these item representations may impart, via Hebbian association^{78,79} of coactive LVCs and place cells, added stability to the place-related representations in the hippocampus.

The fields of LVCs bound to multiple landmarks

Although the hippocampus and MEC both contain cells that display vector coding relative to environmental landmarks, there are

differences between the hippocampal LVCs and the MEC object vector cells. We keep here the terminology used by Deshmukh and Knierim²¹ for hippocampal cells and by Høydal et al.²⁶ for MEC cells, although we consider these cell responses to be very similar across regions, with the hippocampal cells demonstrating greater flexibility across sessions than their MEC counterparts. The MEC object vector cells fire in a vector relationship to all discrete landmarks in an environment²⁶. In contrast, hippocampal LVCs do not respond to all landmarks equally. As previously described²¹, the LV representations can be bound to only a subset of the landmarks in an environment, and the LV firing fields can jump from one landmark to another in different sessions. However, contrary to previous claims^{26,67}, hippocampal LVCs do not necessarily require experience to exhibit their landmark vector properties. Deshmukh and Knierim's²¹ original report stated that, even though their strongest evidence for LVC coding came from the development of new LV fields at predicted locations with experience, it was unclear from their data whether such experience was required. The present results demonstrate that LVCs can be present from the rat's first experience with landmarks, and thus they are similar in this regard to object vector cells of MEC. To avoid confusion between MEC and hippocampal vector coding, we advocate that all such coding in hippocampus follow the landmark vector nomenclature of McNaughton et al.²⁴ (and adopted by Deshmukh and Knierim²¹), who predicted the existence of such properties in the hippocampus.

Regarding the flexibility of LVC binding to different subsets of landmarks across time, the hippocampus receives inputs from two main streams: allocentric spatial information (location, direction, and speed) from the MEC^{4,8,53} and egocentric information about external cues and relative location from the LEC^{80,81}. Like hippocampal LVCs, cells in LEC respond to multiple landmarks, but the firing is inconsistent across sessions²². Thus, the LVC firing of place cells may be driven by the variable landmark-related activity of LEC cells as well as the stable object vector firing of MEC cells, with hippocampal dynamics and plasticity related to both entorhinal inputs likely contributing to the differences between hippocampal inputs and outputs. An open question is how a downstream region knows what landmark the rat is near, if the MEC LVCs fire equally at all landmarks and the LEC and hippocampal cells fire only transiently at discrete subsets of landmarks. One possibility is that the downstream areas can distinguish objects by their locations, by decoding the rat's allocentric location from the population of place cells simultaneously firing in synchrony with the LVCs. Alternatively, it has been argued that population coding of objects in CA1 provides a greater ability to decode object identity than single-cell responses¹⁵.

Vector navigation and vector coding in the hippocampal system

A fundamental question is whether Cartesian or polar coordinate systems are used for LVC and place field representations. Gallistel⁸² has argued that, for path integration navigation, it is more efficient to represent space in a Cartesian system, and much research of place cells implicitly or explicitly assumes that the cognitive map is a Cartesian system. In contrast, vector coding may be more naturally represented in a polar coordinate system of distances and angles. Indeed, O'Keefe⁸³ proposed a model in which spatial representations were based on such a polar coordinate system anchored to the centroid of the available spatial landmarks in an environment. Under this model, like LVCs, place fields may represent location as a vector in a polar coordinate system, anchored to the center of the environment. Such cells are present in the postrhinal cortex⁸⁴ and perhaps LEC⁸⁵.

Recent years have witnessed a rebirth of the notion of vector navigation in rodents and vector representations in the hippocampus and related areas. Inspired by behavioral studies of goal-seeking behavior controlled by vector relationships to individual landmarks¹⁷, McNaughton et al.²⁴ hypothesized that place cells may represent vectors to individual landmarks in an environment. Deshmukh and

Knierim²¹ confirmed this hypothesis, at least for a subset of CA1 place cells in a given environment that fired at a constant vector relationship with multiple landmarks in an environment. These LVCs were similar to boundary vector cells previously identified in the subiculum, which fired in a vector relationship to the animal's position relative to an extended boundary rather than a discrete landmark^{7,27,58}. Subsequently, object vector cells were discovered in the mouse MEC²⁶. In recent years, other forms of egocentric vector cells have been discovered in rat and bat hippocampus^{29,60,86}, rat LEC⁸⁵, rat parietal cortex⁸⁷, rat postsubiculum⁸⁸, rat postrhinal cortex^{84,89}, rat striatum⁹⁰, rat retrosplenial cortex⁹¹, and human hippocampal formation⁹². These cells fire at a distance and are egocentric, bearing to specific items in an environment, such as landmarks, goals, boundaries, and/or the center of the environment. Place cells have also been shown to create a population code for vector navigation²⁸, and deep learning networks trained to perform vector navigation develop grid cell firing properties autonomously⁹³. Thus, the study of vector navigation and vector coding in the hippocampus and related areas is a burgeoning field that promises to reveal fundamental principles underlying the relationship between hippocampal spatial representations and navigation, as well as perhaps episodic memory^{13,85}.

Methods

Subjects

5 male and 3 female adults, Long-Evans rats (Charles River Laboratories, 4–8 months old) were successfully injected in CA1 with AAV9-GCaMP6f, implanted with a 2 mm GRIN lens, and trained to forage for food reward scattered on an open platform (Fig. 1a). Animals were individually housed in an animal facility with a reversed 12 h light-dark cycle, and all recordings were performed in the dark cycle. In our results, there was no significant difference between male and female rats (Supplementary Fig. 5), and thus data from both sexes are combined in analyses. All animal care, surgical, and housing protocols were approved by the Institutional Animal Care and Use Committee at Johns Hopkins University and complied with National Institutes of Health guidelines.

Virus injection

Rats were initially anesthetized with 3% isoflurane, followed by ketamine and xylazine injection; anesthesia was maintained with 0.5–1.5% isoflurane. During the surgery procedure, the depth of the anesthesia was assessed by periodic tests of responsiveness to toe or tail pinch and by monitoring breathing. Animals were placed in a stereotax, an ~2 cm incision was made midline on the scalp, and a small craniotomy (~0.5 mm) was made at the target coordinate (AP: -4.0; ML: 2.7). A Hamilton syringe (Hamilton, Model 1701 SN syringe, Model 1701 SN Syringe, Volume = 10 µl, Point Style: 4, Gauge: 33, Angle: 17, Needle Length: 30 mm) loaded with 3.0 µl AAV9. Syn.GCaMP6f. WPRE.SV40 virus (titer: 4×10^{13} GC per ml, obtained from Addgene) was lowered to a depth of 2.4 mm below the dura. Five minutes after the needle was placed at the target depth, a total of 1.5 µl virus was injected over 20 min. The syringe was left for 15 min before it was slowly withdrawn. After the virus injection, bone wax was applied to the craniotomy. Meloxicam was given subcutaneously at the end of the surgery.

Microendoscope lens implantation

Lens implantation surgery was performed 2 weeks after the virus injection surgery. The anesthesia procedure was identical to that previously described. An incision was made on the rats' scalp, and the periosteum was dissected from the skull. Four screws were screwed into the skull, and a 2 mm diameter craniotomy (center at AP: 4.0 mm; ML: 2.5 mm from bregma) was made. After removing the dura, the tissue was aspirated until the corpus callosum appeared, as indicated by stripes of white matter axons oriented in the medial-lateral axis; saline was continuously applied during the aspiration. A 32 G needle was used to gently

remove the axons of the corpus callosum until the stripes of the alveus axons, oriented in the anterior-posterior axis, fully appeared in the craniotomy. A 2 mm GRIN lens (0.25 pitch, Edmund Optics) was placed at the center of the craniotomy and lowered to a depth of 2.8 mm from the skull. To increase the success rate of the surgery, we checked the quality of the calcium activity signal after the lens was temporarily secured when rats were anesthetized. The lens was cemented in place if robust signals were detected (Supplementary Fig. 1b), and neural recordings commenced two weeks later. Otherwise, a customized virus-coated lens⁹⁴ was inserted to replace the previous one and cemented in place. The lens was secured by applying cyanoacrylate glue surrounding the lens and followed with a thin layer of bone cement (PALACOS, Zimmer) on the skull. The lens was covered with Kwik-Sil (World Precision Instruments). Animals were then given dexamethasone (0.2 mg/kg, subcutaneously) and buprenorphine (0.05 mg/kg, subcutaneously) after surgery. Two to four weeks after the implantation surgery, animals were anesthetized with 2.0–3% isoflurane, and a baseplate was attached with self-adhesive resin cement (3 M) and dental cement (Coltene). A screw-secured cap covered the lens.

Preparation of the virus-coated lens

The virus-coated lenses were prepared one day before the aspiration surgery. The virus was slowly mixed with silk fibroin solution (50 mg/mL, Millipore Sigma) with a ratio of 1:1 through the pipette to avoid generating bubbles. 1 μ L of this mixture was applied on top of the lens surface homogeneously. After the first drop was completely dry, a second coating of 1 μ L was gently applied.

Behavior training and calcium imaging

After rats had recovered from the lens implantation surgery, they were food-restricted to ~85–90% of their free-feeding weight and trained to forage for chocolate pellets on a square open platform (107 \times 107 cm) for 40 minutes per day. In most sessions, the platform contained various numbers of identical landmarks (water bottles wrapped with black tape, 5 cm in diameter and 20 cm high); the number varied based on experimental conditions. When present, the landmarks were placed at the centers of a subset of the platform's four quadrants. Black curtains surrounded the platform, and a cue card (84 \times 114.5 cm) was placed on the north side of the curtain to serve as the only salient orienting cue in the environment.

For the cue card rotation experiment, rats were allowed to rest for 20–25 minutes after the first session. Rats were then placed in a covered box; the experimenter rotated the box smoothly when walking between the common area of the lab and the computer room to disassociate the rats' directional sense from that in the recording room. The covered box with the rat was taken inside the curtain by the experimenter at the entering position that keeps the same relationship with the cue card as in the previous session (the entering position is 180° opposite to the cue card location). Each recording session lasted 20 minutes.

For recordings, the miniscopes (http://miniscope.org/index.php/Main_Page) were secured to the rats' heads, with the rat held at a position 180° opposite to the cue card location. Calcium images (752 \times 480 pixels, V3 miniscope; 608 \times 608 pixels, V4 miniscope; 30 Hz) were collected with the miniscope via a CMOS imaging sensor (Aptina, MT9V032C12) connected to a custom data acquisition system (DAQ). The DAQ was connected to a PC with a USB 3.0 cable and controlled by custom DAQ software. Animal behavioral data was acquired by a webcam at 30 Hz. Both imaging videos and behavioral videos were written to .avi files, and the trajectories of rats were analyzed by offline custom Python and MATLAB code to track the red LED on the CMOS of the miniscope.

Data analysis

Raw videos of calcium images were first concatenated, spatially downsampled by a factor of 2 (376 \times 240 pixels, V3 miniscope;

304 \times 304 pixels, V4 miniscope³³; http://miniscope.org/index.php/Main_Page), temporally downsampled by a factor of 4 (7.5 Hz) by custom MATLAB scripts, and motion-corrected in Matlab with NoRMCorre⁹⁵. Signal extractions, denoising, deconvolving, and demixing were performed by employing a MATLAB package (https://github.com/zhoup/CNMF_E) that uses constrained non-negative matrix factorization for microendoscope (CNMF-E)⁹⁶. This toolbox removes noise and background fluctuations from the raw data and then extracts the neuronal temporal Ca²⁺ activities and spatial footprints. The CNMF-E trace was then detrended and deconvolved to infer the relative amplitudes of spiking events (normalized between 0 and 1) by the fast OOPSI algorithm⁹⁷. A threshold for the minimum event amplitude (typically a *s_min* parameter of -8 was used in the code; the actual threshold is determined by the noise level) was applied to prevent the influence of residual noise from the CNMF-E trace. The normalized spikes with amplitude (calcium events) were used for further analysis in the rate maps. To prevent the spurious detection of overlapping neurons as a single neuron, we employed a number of procedures. For each rat, we chose 2–3 average cells from a single recording session and measured the diameters of the images of their calcium signals through image J⁹⁸. The mean diameter of these cells for each rat was fed as a parameter in CNMF-E. CNMF-E incorporates sparsity constraints that each individual neuron should be represented by only a few spatial components^{96,99}. Temporal smoothing is also incorporated with CNMF-E, which assumes that the activity of a neuron changes smoothly over time to reduce the noise and help isolate different neurons. Moreover, CNMF-E uses an iterative optimization procedure to refine the spatial and temporal components over multiple iterations until convergence is achieved. Images were visually curated, and any oddly shaped neurons that might reflect overlapping cells were either manually segregated into separate cells or discarded from analysis (Supplementary Fig. 1d); the total discarded neuron number was <0.5%. In particular, examples of conjunctive place \times landmarks cells were scrutinized to ensure that the calcium events when the rat was in the place field component came from the same cell as the calcium events when the rat was in the LV field component (Supplementary Movie 2). Finally, CNMF-E applied a post-processing step to remove false positives and merge overlapping neuron components. Those measures help CNMF-E accurately extract signals from individual neurons in the calcium imaging dataset.

Tracking the same cells across sessions and across days

To identify the same cells from images that are recorded from multiple recording sessions, we applied a probabilistic method to automatically register individual cells across multiple imaging sessions and determine the confidence of each registered cell¹⁰⁰. Initially, we applied CNMF-E analysis to produce spatial footprints for all cells captured during the first recording session. Subsequently, the same procedures were repeated for the cells imaged during other sessions within the same day or across the days. To correct for translation and rotation differences among sessions, all sessions were aligned to the first recording session. This alignment allows the spatial footprints' locations from different recording sessions to be in the same coordinate frame (Fig. 1d and Supplementary Fig. 1c). Cells from different sessions were considered to be the same if the distance between their centers of mass was <14 μ m and the Pearson correlation between their spatial footprints was >0.5¹⁰⁰.

Place cell identification

The trajectories of rats were smoothed with a five-frame boxcar filter (150 ms) and filtered by velocity (3 cm/s). The square platform was binned into 3 \times 3 cm spatial bins. The spatial rate map for each neuron was calculated by dividing the total number of calcium events by the animals' total occupancy in each spatial bin. Bins with total occupancy over 0.3 sec were included in the calculation. The map was then

smoothed with a 6-cm Gaussian kernel. To quantify the information content of a given neuron, the spatial information score for each neuron was calculated with the following formula¹⁰¹,

$$\text{Information} = \sum_{i=1}^N P_i \frac{\lambda_i}{\lambda} \log 2 \left(\frac{\lambda_i}{\lambda} \right) \quad (1)$$

where P_i is the probability of the rat occupying i -th bin for the given neuron, λ_i is the neuron's activity rate in the i -th bin (each calcium event is considered as an activity event), and λ is the overall mean rate of the neuron across the entire sessions. The timing of the calcium event was shuffled by shifting a random amount of time (minimum 50 sec) 1000 times, and the spatial information was recalculated for each shuffle. A distribution of 1000 times of shuffled spatial information was generated. A given neuron was classified as an active cell if it had a mean activity rate over 0.01 Hz; and the active cell was classified as a place cell if the observed spatial information was higher than the 95th percentile of the spatial information distribution generated by 1000 shuffles ($p < 0.05$). Calcium imaging experiments in mice showed lower percentages of place cells (20–40%)^{46,102} than those with electrophysiological studies (~47–70%)^{46,103,104}, whereas a previous study using miniscopes in rats reported a higher proportion (77.3%) of place cells³⁵. Unlike the present study, other studies with head-mounted miniscopes used the number of active cells—defined as cells that had a minimum number or rate of calcium transient activity—in the denominator to calculate place cell proportions^{35,46}; this minimum number excluded cells that displayed only a single transient (or a very small number of transients), thereby underestimating the number of cells in the imaging plane. In contrast, we included all cells that fired ≥ 1 transient in the denominator, which, while still underestimating the denominator by excluding cells that fired no transients and were therefore invisible, produced a smaller proportion of cells with place fields that matched more closely the data from single-unit electrophysiology studies.

Computation of LRD and PRD

To compute the LRD for each cell, we extracted the rat's trajectory and calcium signals in circles with a radius of 24 cm centered on the objects in quadrants 1 and 3 (Fig. 4a, left) and created circular firing rate maps. We rotated the rat's trajectory and calcium signals for the standard sessions in circles 1 and 3 in steps of 1° , with the landmark at the center of the circles as the axis of rotation. The rotated combination map was generated by averaging the firing maps generated based on rotated matrices (Rotated 1 and Rotated 3; Fig. 4a, left). The number of bins in which non-zero firing rates overlapped was computed between the rotated combination map in each rotation step and the combination map in the rotation session (Supplementary Fig. 3f, i, l, o, r). The LRD was defined as the peak of the smoothed number of overlap bins using the Savitzky-Golay filter (Supplementary Fig. 3f, i). If there was no overlap between the standard combination map and all rotated combination maps in the second session, the LRD value was assigned a null value and discarded (Supplementary Fig. 3c).

To calculate the PRD, the trajectory and calcium signals in the standard session were rotated with respect to the center of the platform in 1° increments. Subsequently, the rotated rate maps were generated based on the rotated matrices, and the numbers of overlap bins were computed between the rotated rate map in the standard session and the rate map in the rotation session. Finally, we applied the Savitzky-Golay filter to the number of overlap bins for each rotation step to identify the peak, which we defined as PRD (Supplementary Fig. 3b, e, h, k, n, q).

Geometric rotation score

Autocorrelation of the LRD distribution (5° steps) was used to measure the 4-fold, rotational symmetry of this distribution. Analogous to the

standard measure of gridness for grid cells⁵³, the geometric rotation score was computed by taking the minimum correlation values through rotations of 90° , 180° and 270° , from which was subtracted the maximum correlation values through rotations of 45° , 135° , 225° and 315° : Geometric rotation score = $\min(\text{Acorr}_{90^\circ}, \text{Acorr}_{180^\circ}, \text{Acorr}_{270^\circ}) - \max(\text{Acorr}_{45^\circ}, \text{Acorr}_{135^\circ}, \text{Acorr}_{225^\circ})$.

Statistics

All statistical analyses were performed in MATLAB (Mathworks) and GraphPad Prism 9. Results are considered statistically significant when p values are < 0.05 . Functions from the Matlab circular statistics toolbox were used to determine circular statistics¹⁰⁵. The circular analog of the Kruskal-Wallis test (`circ_cmtest`) was used to determine whether there were significant differences between the medians of PRD and LRD. The statistical procedure involving shuffles was repeated 1000 times. All statistical tests other than the shuffle tests were two-sided; the shuffle tests were one-sided, as is typical for these types of tests.

Histological procedures

After the conclusion of the recording, rats were deeply anesthetized with Euthasol and transcardially perfused with 4% PFA prepared in PBS. The lens was carefully removed, and the extracted brain was kept in 4% PFA overnight. The extracted brain was transferred to 30% sucrose in PBS the next day. After >36 hours, the brain was sectioned coronally into 40- μm -thick sections. Brain sections were mounted on glass slides and mounted with the fluorescence mounting medium with DAPI (Vector laboratories). Images were acquired by Zeiss LSM 780 confocal microscope. Damage to the alveus was found in a number of rats, but it was unclear whether this damage resulted from the insertion of the tip of the lens into the alveus or whether it was due to healthy tissue attached to the GRIN lens being damaged during lean removal. We noticed that about half of the rats had large numbers of highly spatially tuned place cells, while the other half had many poorly selective place cells. The latter group typically showed more alveus damage than the former, and we attribute the lack of standard place cell selectivity in these rats to the hippocampal damage from the lens. Thus, we discarded all of the data from rats ($n = 4$) that did not show good place cells during the recordings, leaving the final number of eight rats analyzed in the study.

Reporting summary

Further information on research design is available in the Nature Portfolio Reporting Summary linked to this article.

Data availability

Data supporting this study are available in the GitHub repository at <https://github.com/YueqingZhou/Landmark-vector-cell>. Additional data related to this paper are available upon request to corresponding authors, as the size of the calcium imaging and animal behavioral tracking data is too large for online deposit. Source data are provided with this paper.

Code availability

The analysis code used in this study is available at: <https://github.com/YueqingZhou/Landmark-vector-cell>. Additionally, circular statistical analyses were conducted using the Circular Statistics Toolbox¹⁰⁵: <https://www.mathworks.com/matlabcentral/fileexchange/10676-circular-statistics-toolbox-directional-statistics>.

References

- Etienne, A. S. & Jeffery, K. J. Path integration in mammals. *Hippocampus* **14**, 180–192 (2004).
- Mittelstaedt, M. L. & Mittelstaedt, H. Homing by path integration in a mammal. *Naturwissenschaften* **67**, 566–567 (1980).

3. O'Keefe, J. & Nadel, L. The hippocampus as a cognitive map (Clarendon Press; Oxford University Press, Oxford New York, 1978).
4. Hafting, T., Fyhn, M., Molden, S., Moser, M. B. & Moser, E. I. Microstructure of a spatial map in the entorhinal cortex. *Nature* **436**, 801–806 (2005).
5. Taube, J. S. & Bassett, J. P. Persistent neural activity in head direction cells. *Cereb. Cortex* **13**, 1162–1172 (2003).
6. Knierim, J. J., Kudrimoti, H. S. & McNaughton, B. L. Interactions between idiothetic cues and external landmarks in the control of place cells and head direction cells. *J. Neurophysiol.* **80**, 425–446 (1998).
7. Lever, C., Burton, S., Jeewajee, A., O'Keefe, J. & Burgess, N. Boundary vector cells in the subiculum of the hippocampal formation. *J. Neurosci.* **29**, 9771–9777 (2009).
8. Kropff, E., Carmichael, J. E., Moser, M. B. & Moser, E. I. Speed cells in the medial entorhinal cortex. *Nature* **523**, 419–U478 (2015).
9. Moser, E. I., Moser, M. B. & McNaughton, B. L. Spatial representation in the hippocampal formation: a history. *Nat. Neurosci.* **20**, 1448–1464 (2017).
10. Solstad, T., Boccara, C. N., Kropff, E., Moser, M. B. & Moser, E. I. Representation of geometric borders in the entorhinal cortex. *Science* **322**, 1865–1868 (2008).
11. Savelli, F., Yoganarasimha, D. & Knierim, J. J. Influence of boundary removal on the spatial representations of the medial entorhinal cortex. *Hippocampus* **18**, 1270–1282 (2008).
12. Knierim, J. J. The hippocampus. *Curr. Biol.* **25**, R1116–R1121 (2015).
13. Wang, C., Chen, X. & Knierim, J. J. Egocentric and allocentric representations of space in the rodent brain. *Curr. Opin. Neurobiol.* **60**, 12–20 (2020).
14. Cressant, A., Muller, R. U. & Poucet, B. Failure of centrally placed objects to control the firing fields of hippocampal place cells. *J. Neurosci.* **17**, 2531–2542 (1997).
15. Manns, J. R. & Eichenbaum, H. A cognitive map for object memory in the hippocampus. *Learn. Mem.* **16**, 616–624 (2009).
16. Burke, S. N. et al. The influence of objects on place field expression and size in distal hippocampal CA1. *Hippocampus* **21**, 783–801 (2011).
17. Collett, T. S., Cartwright, B. A. & Smith, B. A. Landmark learning and visuo-spatial memories in gerbils. *J. Comp. Physiol. A* **158**, 835–851 (1986).
18. Cartwright, B. A. & Collett, T. S. Landmark learning in bees - experiments and models. *J. Comp. Physiol.* **151**, 521–543 (1983).
19. Cohen, S. J. et al. The rodent hippocampus is essential for non-spatial object memory. *Curr. Biol.* **23**, 1685–1690 (2013).
20. Larkin, M. C., Lykken, C., Tye, L. D., Wickelgren, J. G. & Frank, L. M. Hippocampal output area CA1 broadcasts a generalized novelty signal during an object-place recognition task. *Hippocampus* **24**, 773–783 (2014).
21. Deshmukh, S. S. & Knierim, J. J. Influence of local objects on hippocampal representations: landmark vectors and memory. *Hippocampus* **23**, 253–267 (2013).
22. Deshmukh, S. S. & Knierim, J. J. Representation of non-spatial and spatial information in the lateral entorhinal cortex. *Front. Behav. Neurosci.* **5**, 69 (2011).
23. Young, B. J., Otto, T., Fox, G. D. & Eichenbaum, H. Memory representation within the parahippocampal region. *J. Neurosci.* **17**, 5183–5195 (1997).
24. McNaughton, B., Knierim, J. & Wilson, M. The cognitive neurosciences. Cambridge, Massachusetts: Massachusetts Institute of Technology (1995).
25. Geiller, T., Fattahi, M., Choi, J. S. & Royer, S. Place cells are more strongly tied to landmarks in deep than in superficial CA1. *Nat. Commun.* **8**, 14531 (2017).
26. Hoydal, O. A., Skytøen, E. R., Andersson, S. O., Moser, M. B. & Moser, E. I. Object-vector coding in the medial entorhinal cortex. *Nature* **568**, 400–404 (2019).
27. Poulter, S., Lee, S. A., Dachtler, J., Wills, T. J. & Lever, C. Vector trace cells in the subiculum of the hippocampal formation. *Nat. Neurosci.* **24**, 266–275 (2021).
28. Ormond, J. & O'Keefe, J. Hippocampal place cells have goal-oriented vector fields during navigation. *Nature* **607**, 741 (2022).
29. Sarel, A., Finkelstein, A., Las, L. & Ulanovsky, N. Vectorial representation of spatial goals in the hippocampus of bats. *Science* **355**, 176–180 (2017).
30. McNaughton, B. L. et al. Deciphering the hippocampal polyglot: the hippocampus as a path integration system. *J. Exp. Biol.* **199**, 173–185 (1996).
31. Muller, R. U., Ranck, J. B. & Taube, J. S. Head direction cells: properties and functional significance. *Curr. Opin. Neurobiol.* **6**, 196–206 (1996).
32. Yoganarasimha, D. & Knierim, J. J. Coupling between place cells and head direction cells during relative translations and rotations of distal landmarks. *Exp. Brain Res.* **160**, 344–359 (2005).
33. Cai, D. J. et al. A shared neural ensemble links distinct contextual memories encoded close in time. *Nature* **534**, 115–118 (2016).
34. Hart, E. E., Blair, G. J., O'Dell, T. J., Blair, H. T. & Izquierdo, A. Chemogenetic modulation and single-photon calcium imaging in anterior cingulate cortex reveal a mechanism for effort-based decisions. *J. Neurosci.* **40**, 5628–5643 (2020).
35. Wirtshafter, H. S. & Disterhoft, J. F. In vivo multi-day calcium imaging of CA1 hippocampus in freely moving rats reveals a high preponderance of place cells with consistent place fields. *J. Neurosci.* **42**, 4538–4554 (2022).
36. Wirtshafter, H. S. & Disterhoft, J. F. Place cells are nonrandomly clustered by field location in CA1 hippocampus. *Hippocampus* **33**, 65–84 (2023).
37. Gobbo, F. et al. Neuronal signature of spatial decision-making during navigation by freely moving rats by using calcium imaging. *Proc. Natl Acad. Sci. USA* **119**, e2212152119 (2022).
38. Blair, G. J. et al. Hippocampal place cell remapping occurs with memory storage of aversive experiences. *Elife* **12**, e80661 (2023).
39. Wilson, M. A. & McNaughton, B. L. Dynamics of the hippocampal ensemble code for space. *Science* **261**, 1055–1058 (1993).
40. Kinsky, N. R., Sullivan, D. W., Mau, W., Hasselmo, M. E. & Eichenbaum, H. B. Hippocampal place fields maintain a coherent and flexible map across long timescales. *Curr. Biol.* **28**, 3578–3588.e3576 (2018).
41. Zhou, H. et al. Cholinergic modulation of hippocampal calcium activity across the sleep-wake cycle. *Elife* **8**, e39777 (2019).
42. Guzowski, J. F., McNaughton, B. L., Barnes, C. A. & Worley, P. F. Environment-specific expression of the immediate-early gene Arc in hippocampal neuronal ensembles. *Nat. Neurosci.* **2**, 1120–1124 (1999).
43. Talbot, Z. N. et al. Normal CA1 place fields but disorganized network discharge in a Fmr1-null mouse model of fragile X syndrome. *Neuron* **97**, 684–697.e684 (2018).
44. Witharana, W. K. L. et al. Nonuniform allocation of hippocampal neurons to place fields across all hippocampal subfields. *Hippocampus* **26**, 1328–1344 (2016).
45. Rich, P. D., Liaw, H. P. & Lee, A. K. Large environments reveal the statistical structure governing hippocampal representations. *Science* **345**, 814–817 (2014).
46. Ziv, Y. et al. Long-term dynamics of CA1 hippocampal place codes. *Nat. Neurosci.* **16**, 264–266 (2013).
47. Muller, R. U. & Kubie, J. L. The effects of changes in the environment on the spatial firing of hippocampal complex-spike cells. *J. Neurosci.* **7**, 1951–1968 (1987).

48. Bostock, E., Muller, R. U. & Kubie, J. L. Experience-dependent modifications of hippocampal place cell firing. *Hippocampus* **1**, 193–205 (1991).
49. Yoganarasimha, D., Yu, X. & Knierim, J. J. Head direction cell representations maintain internal coherence during conflicting proximal and distal cue rotations: comparison with hippocampal place cells. *J. Neurosci.* **26**, 622–631 (2006).
50. Knight, R. et al. Weighted cue integration in the rodent head direction system. *Philos. T R. Soc. B* **369**, 20120512 (2014).
51. Knierim, J. J., Kudrimoti, H. S. & McNaughton, B. L. Place cells, head direction cells, and the learning of landmark stability. *J. Neurosci.* **15**, 1648–1659 (1995).
52. Taube, J. S. The head direction signal: origins and sensory-motor integration. *Annu. Rev. Neurosci.* **30**, 181–207 (2007).
53. Sargolini, F. et al. Conjunctive representation of position, direction, and velocity in entorhinal cortex. *Science* **312**, 758–762 (2006).
54. Thompson, L. T. & Best, P. J. Long-term stability of the place-field activity of single units recorded from the dorsal hippocampus of freely behaving rats. *Brain Res.* **509**, 299–308 (1990).
55. Mankin, E. A. et al. Neuronal code for extended time in the hippocampus. *Proc. Natl Acad. Sci. USA* **109**, 19462–19467 (2012).
56. Bourboulou, R. et al. Dynamic control of hippocampal spatial coding resolution by local visual cues. *Elife* **8**, e44487 (2019).
57. GoodSmith, D. et al. Flexible encoding of objects and space in single cells of the dentate gyrus. *Curr. Biol.* **32**, 1088–1101.e5 (2022).
58. O’Keefe, J. & Burgess, N. Geometric determinants of the place fields of hippocampal neurons. *Nature* **381**, 425–428 (1996).
59. McNaughton, B. L., Leonard, B. & Chen, L. Cortical-hippocampal interactions and cognitive mapping - a hypothesis based on reintegration of the parietal and inferotemporal pathways for visual processing. *Psychobiology* **17**, 236–246 (1989).
60. Jercog, P. E. et al. Heading direction with respect to a reference point modulates place-cell activity. *Nat. Commun.* **10**, 2333 (2019).
61. Acharya, L., Aghajani, Z. M., Vuong, C., Moore, J. J. & Mehta, M. R. Causal influence of visual cues on hippocampal directional selectivity. *Cell* **164**, 197–207 (2016).
62. Rubin, A., Yartsev, M. M. & Ulanovsky, N. Encoding of head direction by hippocampal place cells in bats. *J. Neurosci. J. Soc. Neurosci.* **34**, 1067–1080 (2014).
63. Gothard, K. M., Skaggs, W. E. & McNaughton, B. L. Dynamics of mismatch correction in the hippocampal ensemble code for space: Interaction between path integration and environmental cues. *J. Neurosci.* **16**, 8027–8040 (1996).
64. Knierim, J. J. & Hamilton, D. A. Framing spatial cognition: neural representations of proximal and distal frames of reference and their roles in navigation. *Physiol. Rev.* **91**, 1245–1279 (2011).
65. Hardcastle, K., Ganguli, S. & Giocomo, L. M. Environmental boundaries as an error correction mechanism for grid cells. *Neuron* **86**, 827–839 (2015).
66. Keinath, A. T., Epstein, R. A. & Balasubramanian, V. Environmental deformations dynamically shift the grid cell spatial metric. *Elife* **7**, e3816 (2018).
67. Nagelhus, A., Andersson, S. O., Cogno, S. G., Moser, E. I. & Moser, M. B. Object-centered population coding in CA1 of the hippocampus. *Neuron* **111**, 2091–2104.e14 (2023).
68. Fyhn, M., Hafting, T., Treves, A., Moser, M. B. & Moser, E. I. Hippocampal remapping and grid realignment in entorhinal cortex. *Nature* **446**, 190–194 (2007).
69. MacDonald, C. J., Lepage, K. Q., Eden, U. T. & Eichenbaum, H. Hippocampal “time cells” bridge the gap in memory for discontinuous events. *Neuron* **71**, 737–749 (2011).
70. Taube, J. S. Head direction cells and the neurophysiological basis for a sense of direction. *Prog. Neurobiol.* **55**, 225–256 (1998).
71. Taube, J. S., Muller, R. U. & Ranck, J. B. Head-direction cells recorded from the postsubiculum in freely moving rats. 1. Description and quantitative-analysis. *J. Neurosci.* **10**, 420–435 (1990).
72. Clark, B. J., Harris, M. J. & Taube, J. S. Control of anterodorsal thalamic head direction cells by environmental boundaries: Comparison with conflicting distal landmarks. *Hippocampus* **22**, 172–187 (2012).
73. Knight, R., Hayman, R., Ginzberg, L. L. & Jeffery, K. Geometric cues influence head direction cells only weakly in nondisoriented rats. *J. Neurosci.* **31**, 15681–15692 (2011).
74. Weiss, S. et al. Consistency of spatial representations in rat entorhinal cortex predicts performance in a reorientation task. *Curr. Biol.* **27**, 3658 (2017).
75. Zhang, N. Y., Grieves, R. M. & Jeffery, K. J. Environment symmetry drives a multidirectional code in rat retrosplenial cortex. *J. Neurosci.* **42**, 9227–9241 (2022).
76. Muller, R. U., Kubie, J. L. & Ranck, J. B. Jr. Spatial firing patterns of hippocampal complex-spike cells in a fixed environment. *J. Neurosci.* **7**, 1935–1950 (1987).
77. Keinath, A. T., Mosser, C. A. & Brandon, M. P. The representation of context in mouse hippocampus is preserved despite neural drift. *Nat. Commun.* **13**, 2415 (2022).
78. Muller, R. U. & Stead, M. Hippocampal place cells connected by Hebbian synapses can solve spatial problems. *Hippocampus* **6**, 709–719 (1996).
79. Jeffery, K. J. & Hayman, R. Plasticity of the hippocampal place cell representation. *Rev. Neurosci.* **15**, 309–331 (2004).
80. Knierim, J. J., Neunuebel, J. P. & Deshmukh, S. S. Functional correlates of the lateral and medial entorhinal cortex: objects, path integration and local-global reference frames. *Philos. Trans. R. Soc. Lond. Ser. B Biol. Sci.* **369**, 20130369 (2014).
81. Lisman, J. E. Role of the dual entorhinal inputs to hippocampus: a hypothesis based on cue/action (non-self/self) couplets. *Prog. Brain Res.* **163**, 615 (2007).
82. Gallistel, C. R. The organization of learning (The MIT Press, 1990).
83. O’Keefe, J. An allocentric spatial model for the hippocampal cognitive map. *Hippocampus* **1**, 230–235 (1991).
84. LaChance, P. A., Todd, T. P. & Taube, J. S. A sense of space in postrhinal cortex. *Science* **365**, eaax4192 (2019).
85. Wang, C. et al. Egocentric coding of external items in the lateral entorhinal cortex. *Science* **362**, 945–949 (2018).
86. Purandare, C. S. et al. Moving bar of light evokes vectorial spatial selectivity in the immobile rat hippocampus. *Nature* **602**, 461 (2022).
87. Wilber, A. A., Clark, B. J., Forster, T. C., Tatsuno, M. & McNaughton, B. L. Interaction of egocentric and world-centered reference frames in the rat posterior parietal cortex. *J. Neurosci.* **34**, 5431–5446 (2014).
88. Peyrache, A., Schieferstein, N. & Buzsaki, G. Transformation of the head-direction signal into a spatial code. *Nat. Commun.* **8**, 1752 (2017).
89. Gofman, X. et al. Dissociation between postrhinal cortex and downstream parahippocampal regions in the representation of egocentric boundaries. *Curr. Biol.* **29**, 2751 (2019).
90. Hinman, J. R., Chapman, G. W. & Hasselmo, M. E. Neuronal representation of environmental boundaries in egocentric coordinates. *Nat. Commun.* **10**, 2772 (2019).
91. Alexander, A. S. et al. Egocentric boundary vector tuning of the retrosplenial cortex. *Sci. Adv.* **6**, eaaz2322 (2020).
92. Kunz, L. et al. A neural code for egocentric spatial maps in the human medial temporal lobe. *Neuron* **109**, 2781–2796.e2710 (2021).

93. Banino, A. et al. Vector-based navigation using grid-like representations in artificial agents. *Nature* **557**, 429 (2018).
94. Jackman, S. L. et al. Silk fibroin films facilitate single-step targeted expression of optogenetic proteins. *Cell Rep.* **22**, 3351–3361 (2018).
95. Pnevmatikakis, E. A. & Giovannucci, A. NoRMCorre: an online algorithm for piecewise rigid motion correction of calcium imaging data. *J. Neurosci. Methods* **291**, 83–94 (2017).
96. Zhou, P. et al. Efficient and accurate extraction of in vivo calcium signals from microendoscopic video data. *Elife* **7**, e28728 (2018).
97. Jewell, S. W., Hocking, T. D., Fearnhead, P. & Witten, D. M. Fast nonconvex deconvolution of calcium imaging data. *Biostatistics* **21**, 709–726 (2020).
98. Schneider, C. A., Rasband, W. S. & Eliceiri, K. W. NIH image to ImageJ: 25 years of image analysis. *Nat. Methods* **9**, 671–675 (2012).
99. Pnevmatikakis, E. A. et al. Simultaneous denoising, deconvolution, and demixing of calcium imaging data. *Neuron* **89**, 285–299 (2016).
100. Sheintuch, L. et al. Tracking the same neurons across multiple days in Ca²⁺ imaging data. *Cell Rep.* **21**, 1102–1115 (2017).
101. Skaggs, W. E., McNaughton, B. L., Wilson, M. A. & Barnes, C. A. Theta phase precession in hippocampal neuronal populations and the compression of temporal sequences. *Hippocampus* **6**, 149–172 (1996).
102. Indersmitten, T. et al. In vivo calcium imaging reveals that cortisol treatment reduces the number of place cells in Thy1-GCaMP6f transgenic mice. *Front. Neurosci.* **13**, 176 (2019).
103. Stefanini, F. et al. A distributed neural code in the dentate gyrus and in CA1. *Neuron* **107**, 703 (2020).
104. Jun, H. et al. Disrupted place cell remapping and impaired grid cells in a knockin model of Alzheimer's disease. *Neuron* **107**, 1095 (2020).
105. Berens, P. CircStat: a MATLAB toolbox for circular statistics. *J. Stat. Softw.* **31**, 1–21 (2009).

Acknowledgements

We thank Daniel Aharoni, Garrett Blair, Tad Blair, Cheng Wang, and the UCLA miniscope project for assistance with applying miniscope technology in rats. We thank Maggie Jiang for her assistance with animal training. This study was funded by grants U01 NS111695 and R01 NS039456 to J.J.K. from the U.S. Public Health Service.

Author contributions

J.J.K., Y.Z., and V.P. designed the experiments. J.J.K. supervised all aspects of the experiments and analysis. Y.Z., J.L.L., and X.C. optimized

the surgical procedure to utilize miniscopes in rats. Y.Z. and L.Z. performed in vivo calcium imaging recordings. Y.Z. and X.C. developed codes to analyze imaging data. Y.Z. performed the computational analyses and prepared the figures. Y.Z. wrote the manuscripts with J.J.K. All authors commented on the final manuscript.

Competing interests

The authors declare no competing interests.

Additional information

Supplementary information The online version contains supplementary material available at <https://doi.org/10.1038/s41467-024-54935-2>.

Correspondence and requests for materials should be addressed to Yue-Qing Zhou or James J. Knierim.

Peer review information *Nature Communications* thanks Francesco Gobbo, and the other, anonymous, reviewers for their contribution to the peer review of this work. A peer review file is available.

Reprints and permissions information is available at <http://www.nature.com/reprints>

Publisher's note Springer Nature remains neutral with regard to jurisdictional claims in published maps and institutional affiliations.

Open Access This article is licensed under a Creative Commons Attribution-NonCommercial-NoDerivatives 4.0 International License, which permits any non-commercial use, sharing, distribution and reproduction in any medium or format, as long as you give appropriate credit to the original author(s) and the source, provide a link to the Creative Commons licence, and indicate if you modified the licensed material. You do not have permission under this licence to share adapted material derived from this article or parts of it. The images or other third party material in this article are included in the article's Creative Commons licence, unless indicated otherwise in a credit line to the material. If material is not included in the article's Creative Commons licence and your intended use is not permitted by statutory regulation or exceeds the permitted use, you will need to obtain permission directly from the copyright holder. To view a copy of this licence, visit <http://creativecommons.org/licenses/by-nc-nd/4.0/>.

© The Author(s) 2024